Multi-scale modeling of ionic electrospray emission 🄵

ⓘD Jeffrey Asher, ⓘD Ziyu Huang, ⓘD Chen Cui, et al.

COLLECTIONS

Paper published as part of the special topic on Physics of Electric Propulsion

🄵   This paper was selected as Featured

View Online   Export Citation   CrossMark

ARTICLES YOU MAY BE INTERESTED IN

Electrospray propulsion: Modeling of the beams of droplets and ions of highly conducting propellants
Journal of Applied Physics **131**, 013307 (2022); https://doi.org/10.1063/5.0073380

The role of secondary species emission in vacuum facility effects for electrospray thrusters
Journal of Applied Physics **130**, 143301 (2021); https://doi.org/10.1063/5.0063476

Multiscale modeling of fragmentation in an electrospray plume
Journal of Applied Physics **130**, 184903 (2021); https://doi.org/10.1063/5.0064711

Multi-scale modeling of ionic electrospray emission (F)

View Online   Export Citation   CrossMark

Jeffrey Asher, [ID] Ziyu Huang, [ID] Chen Cui, [ID] and Joseph Wang[a)] [ID]

AFFILIATIONS

Department of Astronautical Engineering, University of Southern California, Los Angeles, California 90089, USA

Note: This paper is part of the Special Topic on Physics of Electric Propulsion.
[a)]**Author to whom correspondence should be addressed:** josephjw@usc.edu

ABSTRACT

The physics of ionic electrospray propulsion spans multiple length scales. This paper combines a molecular dynamics model, a particle–particle model, and a particle-in-cell model to investigate the physics of ionic electrospray propulsion over 9 orders of magnitude in length scale. The combined models are applied to simulate beam emission for an ionic electrospray propulsion system with porous emitter tips and 1-ethyl-3-methylimidazolium tetrafluoroborate ionic liquid propellant from the emission site to the downstream plume. Additionally, the impact of multiple emission sites from a single emitter tip is analyzed with regard to extractor grid interception and overall beam neutralization for bipolar thruster pairs. Results show that beams consisting of species of different masses (i.e., monomer and dimer species) are affected by particle–particle forces during acceleration and should not be treated as a superposition of independently accelerated species in macro-scale plume models. The activation of multiple emission sites also causes a noticeable increase in the beam's spread, leading to increased intercepted current but relatively little adverse effects in the downstream plume region.

I. INTRODUCTION

Future space missions are increasingly looking to leverage smaller, lighter, and simpler space platforms for complex missions. Miniaturized electric propulsion (EP) is a key enabling technology for these platforms as they allow for greater on-orbit maneuverability. Ionic electrospray propulsion is a novel miniaturized EP technology.[1–5] Electrospray thrusters are electrostatic propulsion devices that generate thrust by extracting and accelerating ions directly from a conductive liquid ion source. The physics of ion emission from a conductive liquid was first described by Taylor[6] with his eponymous Taylor cone. Emission from a Taylor cone can produce charged particles ranging from large droplets to individual ions or any combination therein.[7] Ionic electrospray thrusters refer to a subset of electrospray that are specifically designed to emit primarily in the pure ion regime, first developed by Courtney and Coffman.[8–10]

The mechanical construction of electrospray thrusters is relatively simple compared to other legacy electric propulsion devices. The primary components include an emission site, windowed extractor electrode, and a propellant delivery mechanism. To achieve ionic emission, ionic electrospray thrusters often leverage a porous substrate to deliver propellant to the emission site passively via capillary Laplace pressure. The pores serve a dual-purpose by also providing an anchor point for Taylor cones to form. The porous substrate is fashioned into distinct conical or columnar emitter tips through a variety of means, including laser ablation,[10] acid etching,[11] or conventional micro-machining.[1] Multiple emitter tips are often grouped together into an array of 10s to 100s to provide meaningful thrust.

A major lifetime-limiting component of electrospray thrusters is the windowed extractor grid. Large amounts of direct impingement from the ion beam can result in erosion and contamination of the grid.[12] Contamination of ionic electrospray grids due to intercepted current has been observed experimentally.[13–15] As a result, the characterization of electrospray emission and acceleration physics is critical to further improve system reliability. Grid erosion mechanisms and its adverse affects have been studied extensively for gridded ion thrusters.[16–20] Electrospray thrusters share some of these same concerns. A major concern is grid contamination causing electrostatic discharge and electrical short circuits. The activation of secondary emission sites on an individual emitter tip can drastically exacerbate this process. The primary

intent when designing electrospray thrusters is to form a single emission site per emitter tip that is centered and parallel to the window normal. Operating thrusters at higher voltages provides a higher specific impulse but also potentially leads to the activation of secondary emission sites. Due to randomness in the porous substrate, it is impossible to know exactly when or where a secondary emission site will appear without rigorous laboratory characterization. Often, secondary emission sites are off center from the peak of the emitter tip and, as a result, can experience electric fields that are off-axis. The activation of secondary emission sites often coincides with a drastic increase in intercepted current and off-axis emission.[21]

To date, numerical modeling and simulation studies have mostly focused on characterizing individual physical phenomena at their respective scales of interest. These individual phenomena include pure ion emission from a Taylor cone, particle acceleration, and downstream plume dynamics and neutralization. Figure 1 displays a graphic of the relevant regions of interest, comparable to those previously determined by Wirz *et al.*[22]

The physics of Taylor cone emission has been extensively studied through the use of nonreactive molecular dynamics (MD) simulations. MD simulations have been applied to characterize cone formation and emission properties for colloidal, mixed-mode, and pure ionic emission.[23–29] The MD based modeling are typically limited to the immediate region of emission. Recent studies have also attempted to link the effects of the emitted beam's electric field strength and space charge in the acceleration region to emission characteristics.[23]

Ion acceleration physics has been studied extensively for both ionic and colloidal electrospray thrusters to understand the interactions between charged droplets or ions as they are emitted from the Taylor cone and accelerated out of the thruster exit plane.[12,30]

Particle–Particle (PP) models have been applied to characterized ion beam development within the acceleration region for colloid thrusters.[31] Particle-in-Cell (PIC) models have also been applied to analyze the thruster acceleration region for pure ion emission.[32]

Substantial PIC simulations studies have been carried out on the downstream plume dynamics and related plume neutralization and contamination issues for ion thrusters and Hall thrusters (for example, see Refs. 33–38, and references therein). PIC simulations have also been applied to study FEEP thruster beam neutralization and plume interactions.[39–42] Electrospray thrusters offer the additional ability to self-neutralize through the use of bipolar thruster pairs.[43] This self-neutralization entails one thruster emitting a positive cation beam and a second thruster emitting a negative anion beam. Recently, a full-particle PIC model was introduced to understand the unique neutralization process offered by operating a bipolar pair of ionic electrospray thrusters.[44–46] These previous models, however, made several assumptions regarding the properties of the emitted beams that are affected by small scale interactions.

The physics of ionic electrospray emission is affected by interactions occurring in concert over 9 orders of magnitude in length scales: the spatial scale of the emission site is of the order of nanometers (nm), that of the acceleration region is micro-meter ($\sim\mu$m), and that of the plume region is from centimeter (cm) to meter (m). To better understand the full spectrum of physical interactions of an ionic electrospray thruster, a multi-scale simulation study is required. This paper presents a consistent simulation of pure ionic emission from a porous emitter tip by combining a MD model for beam emission at O (nm), a PP model for ion interaction and acceleration at O (μm), and a PIC model for plume neutralization at O (cm)–O (m).

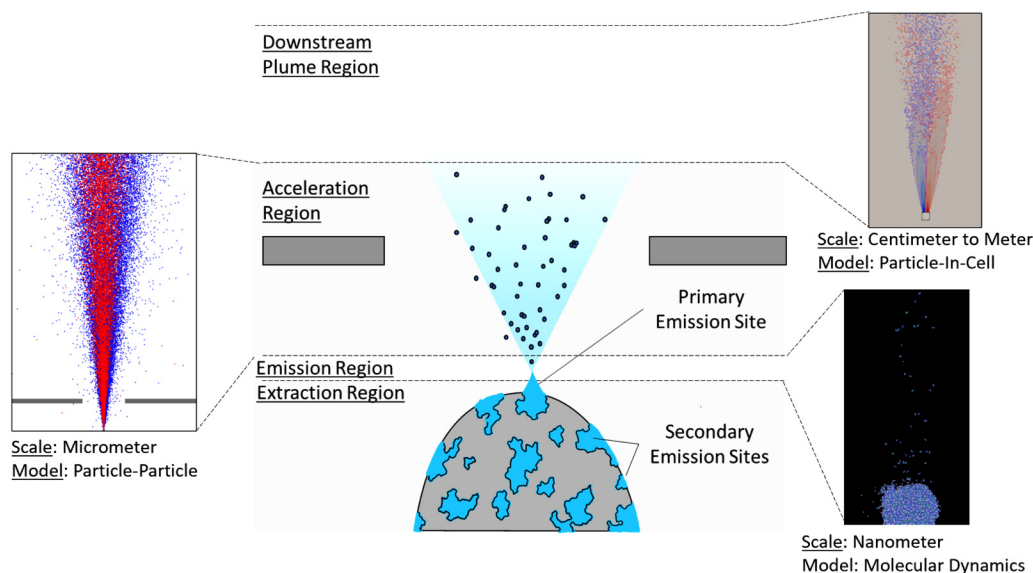In this paper, the combined MD, PP, and PIC models are applied to simulate beam emission of the USC Testbed Thruster

FIG. 1. Scale of electrospray regions and modeling approach.

(UTT).[47] UTT is comparable in design to that of AFRL's AFET-II.[1] Results from each sub-model are compared to highlight key physical interactions at each scale. The resulting downstream plume and neutralization dynamics are also compared to previous results.[46] In addition, a case study is presented to better understand the impact of secondary emission site activation on grid impingement and overall plume neutralization.

II. SIMULATION MODEL AND APPROACH

The simulation model is composed of three sub-models: a MD model for ion emission, a PP model for ion acceleration, and a PIC model for beam neutralization and plume structure. In simulations, the MD model is first applied to determine the plume composition (i.e., percentage of monomer, dimer, or trimer species) as well as a representative 3D velocity distribution function in an extracting electric field. The PP model is then used to resolve the forces on the emitted particles due to the background electric field and particle–particle forces. Last, the distributions generated from both positive cation and negative anion emission are injected into the PIC model to understand bipolar thruster pair neutralization. In the PP and PIC models, the immersed-finite-element (IFE) field solver[48,49] is used to solve the electric field generated by a complex shaped, biased dielectric, or conducting surface, such as the emitter tip and extractor electrode. This section describes these models in detail as well as their key assumptions and interfaces.

A. Molecular dynamics model

The MD model is applied to simulate the emission process at the emission sites on the porous emitter surface, investigating the physics at a length scale of O (1–100 nm). MD simulation is a first principle based modeling method that treats each molecule as a particle and calculates inter-molecular based on the position of atoms and their associated force field. By implementing an accurate force field between particles and integrating the Newtonian equations of motion, we can solve for the interactions between atoms during the electrospray emission process. In this paper, we used Groningen Machine for Chemical Simulations (GROMACS)[50] to simulate the interactions between ionic liquid molecules. GROMACS was originally designed to capture the force fields of complicated bonded interactions of biochemical molecules and has been recently applied to the MD studies of ionic liquids. The potential of each atom is shown in Eq. (1),

$$
\begin{aligned}
V = &\sum_{\text{bonds}} \frac{1}{2} k_{\text{bonds}} (r - r_0)^2 + \sum_{\text{angles}} \frac{1}{2} k_{\text{angles}} (\theta - \theta_0)^2 \\
&+ \sum_{\text{torsions}} \frac{1}{2} (V_1 (1 + \cos \varphi) + V_2 (1 - \cos 2\varphi) \\
&+ V_3 (1 + \cos 3\varphi) + V_4 (1 - \cos 4\varphi)) \\
&+ \sum_{\text{Coloumb}}^{i<j} \frac{q_i q_j}{r_{ij}} + \sum_{\text{vdW}}^{i<j} \left\{ 4\varepsilon_{ij} \left[\left(\frac{\sigma_{ij}}{r_{ij}} \right)^{12} - \left(\frac{\sigma_{ij}}{r_{ij}} \right)^6 \right] \right\},
\end{aligned}
\tag{1}
$$

where k_{bonds} is the constant of bond potential, k_{angles} is the force constant for potential induced by angular differences, V_1, V_2, V_3,
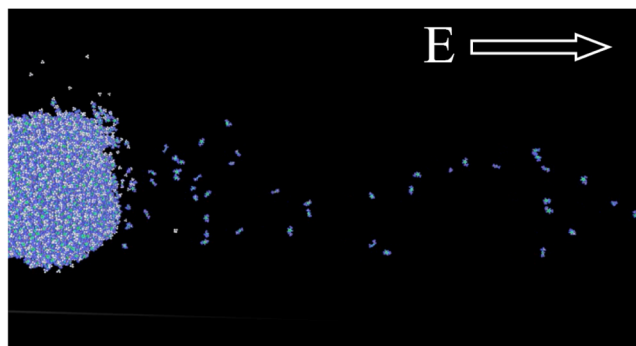

FIG. 2. MD emission of monomer and dimer species from an applied electric field.

and V_4 are Fourier coefficients for each dihedral, and ϵ_{ij} is the constant for the Lennard-Jones potential.

The MD model is constructed using Large-scale Atomic/Molecular Massively Parallel Simulator (LAMMPS).[51] The model considers a column of EMI$^+$ and BF$_4^-$ molecules that is allowed to relax to form 1-ethyl-3-methylimidazolium tetrafluoroborate (EMI-BF$_4$) from the tip of the Taylor cone. An external electric field is applied to the top 20 Å, achieving emission. Figure 2 portrays the MD emission model emitting a positive cation beam. The simulation domain is held at a constant volume of $6000 \times 400 \times 400$ nm. The total number of atoms used is 144 000, with 6000 EMI-BF$_4$ molecules. These 6000 EMI-BF$_4$ molecules provide a large reservoir of neutral molecules to establish steady emission results over the simulation time period. A fraction of these molecules are emitted in the simulation. These emitted molecules correspond directly to every physical molecule emitted from an emission site.

Taylor cone emission starts once the electric field exceeds the emission threshold of about ± 1 V/nm.[27,52,53] The electric field at an emission site is determined not only by its location on the emitter tip but also by the size and shape of the specific pore-propellant interface. This interface cannot be known exactly due to the randomness of pore size/shape on the emitter surface after tip manufacturing processes.[1,10,11] It has been observed that emission at electric fields $> \pm 2$ V/nm significantly reduces the dimer population entering the acceleration region.[27,52,53] As experimental characterization activities have detected the presence of a large proportion (up to 50%) of the dimer species,[1–3] the MD simulations considered positive cation and negative anion emission across a variety of applied electric fields ranging from ± 1 V/nm to ± 2 V/nm.

The emitted particles are sampled to create representative particle velocity distribution functions used in the PP model. The simulation time step is set to 1 fs to ensure the inter-molecular interactions are fully resolved. Each simulation case consists of 10^6 total steps and takes about 12 h of run time on USC's high performance computer (HPC).

B. Immersed-finite-element field solver

The PP model considers emission from a single micro-machined porous emitter tip. The emitter tip is modeled as a

dielectric cone 300μm tall with a 75° slope. The tip of the cone is rounded with a radius of curvature of 14μm. The extractor grid is circular and assumed to be level with the vertex of the cone, 49μm above the emitter tip. The extractor window is 508μm in diameter. This geometry is consistent with previously published designs[1] and is displayed in Fig. 3. The average pore size of the substrate is 1μm, consistent with P5 glass. It is the pores near the tip that will be possible Taylor cone emission sites.

The background electric field generated by such a structure is solved using the IFE field solver. This model is capable of solving the electric field and object charging self-consistently for complex shaped objects and had been previously applied to analyze a variety of electrostatic interaction problems, such as that for charged composite materials[48] and lunar regolith surface.[49] Here, we consider a dielectric glass tip with a permittivity equal to $30\varepsilon_0$. The $-Z$ boundary is set to $\pm 1\,500$ V with a Dirichlet boundary condition. All other external boundaries satisfy the Neumann boundary condition. The extractor grid window is set to 0 V and is assumed a perfect conductor. We use a uniform mesh of cell size $5 \times 5 \times 1 \mu$m^3 to resolve the geometric features of the emitter tip and extractor grid in sufficient detail. The domain measures $201 \times 201 \times 701$ cells. The background field is able to be solved with approximately 1.5 h of runtime on the USC HPC.

Figures 4 and 5 display the background electric field in the acceleration region, subject to the potential applied at the bottom plate of the emitter and the extractor grid, for the positive beam emission case. The background electric field is solved up to the resolution of the IFE mesh size, $dx = dy = 5 \mu$m and $dz = 1 \mu$m. The results show that the maximum electric field strength is localized to the apex of the emitter tip and falls off drastically moving toward the base. While computation limitation does not allow the IFE model to resolve the electric field at the nm scale, we find the electric field strength around the apex of the tip is of the same order of magnitude of the emission threshold and correlates with the likelihood of Taylor cone emission sites being activated at that location.

C. Particle–particle model

The PP model is applied to simulate the ion acceleration region around an emitter, investigating the physics at a length scale of $O(1 \mu$m–1 mm$)$. The PP model is extended from a PP model previously developed to investigate droplet acceleration in colloid electrospray thrusters[31] and ion thruster beam neutralization.[54] One may consider the PP model as a reduced MD model focusing on the Coulomb interactions between charged particles. A PP model does not use a mesh and calculates the electrostatic forces on particles directly from Coulomb's law between each particle pair. The total force on each particle in the domain is described as the sum of the external background electric field and the summation of all particle–particle forces. Therefore, the system of
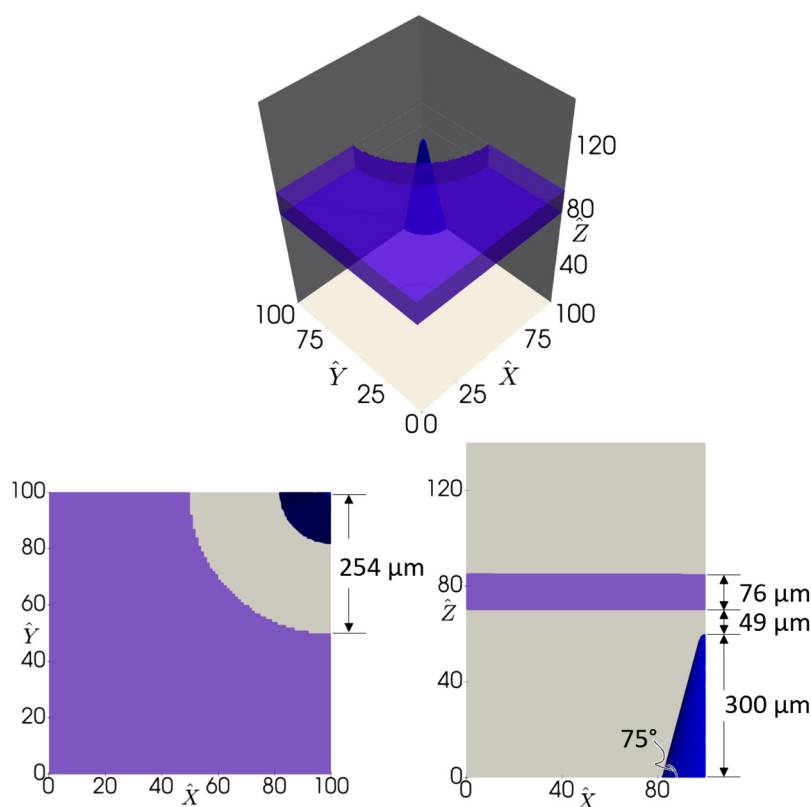

FIG. 3. The geometry of the emitter tip and extractor grid for calculating background field properties.
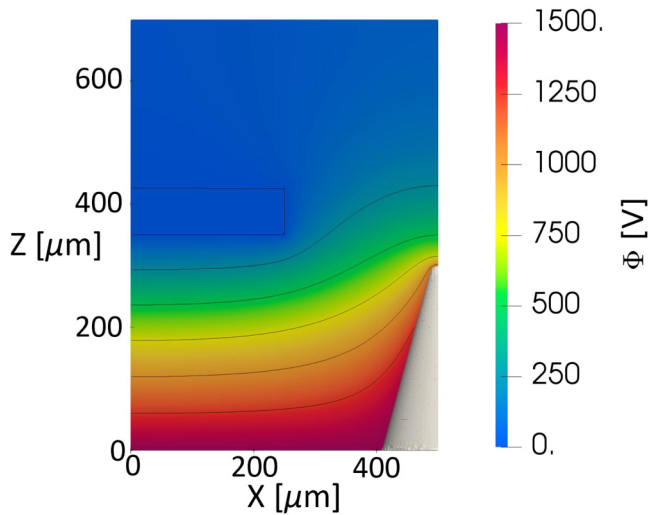
FIG. 4. Background electric potential in the acceleration region for the positive emission case.

equations for particle motion is described in Eq. (2),

$$m\frac{d^2\mathbf{r}}{dt^2} = m\frac{d\mathbf{v}}{dt} = \mathbf{F} = \mathbf{F}_{pp} + \mathbf{F}_{acc} = q(\mathbf{E}_{pp} + \mathbf{E}_{acc}),\quad(2)$$

where q represents the particle charge, $\mathbf{E}_{pp}$ refers to the electric field due to particle–particle forces as described in Eq. (3), and $\mathbf{E}_{acc}$ refers to the background electric field. The background electric field is solved by the IFE field solver. The result is interpolated to the
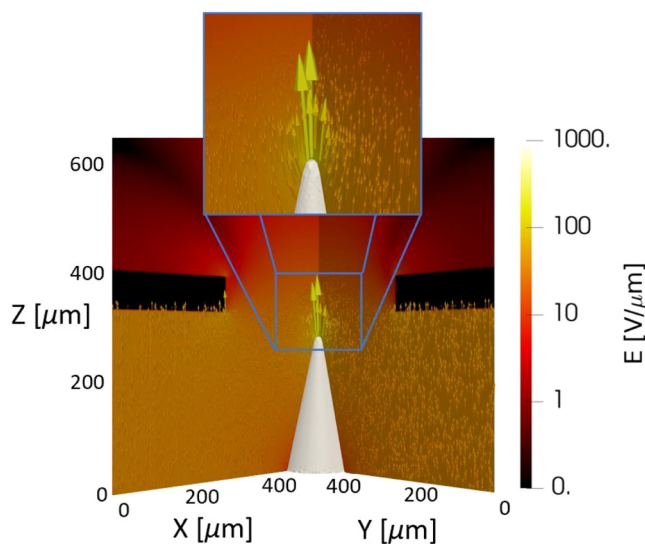

FIG. 5. Background electric field strength in the acceleration region for the positive emission case.

particle locations in the PP model using a linear force weighting scheme,

$$\mathbf{E}_{pp}^{(i)} = \frac{1}{4\pi\epsilon_0}\sum_{j=1,i\neq j}^{N}\frac{q_j}{|\mathbf{r_{ij}}|^3}\mathbf{r_{ij}}.\quad(3)$$

The PP method is typically not as computationally efficient as PIC because its computation scales as $O(N^2)$, where N is the number of particles in the simulation. However, to resolve the ion acceleration process over a region of O (1 mm³) with a resolution of O (1 μm), a PIC model would spend most of its computing time on solving the elliptical Poisson's equation due to the domain mesh size. Since the PP approach does not use a mesh and thus eliminates field-solve and particle-mesh interpolation, PP is computationally more efficient than PIC for this application.[54]

The PP model links to the MD model by generating injected particles using the composition percentage, the velocity distribution function, and the emission rate produced by the MD emission model. Table I displays other relevant input parameters used to setup the PP model. The simulation time step is set to 1 ps. The PP simulation is ended when a statistically representative number of particles have entered the downstream region, at approximately 1 mm from the thruster exit plane. The amount of time required to achieve this result varies with particle species and velocities. A typical simulation case generates up to 60 000 particles, executes a total of 2000 time steps and takes about 10 h of computation time on the USC HPC.

D. Particle-in-cell model

The PIC model is applied to simulate beam neutralization and plume structure, investigating the physics at a length scale of O (1 cm–1 m). The PIC simulation model is extended from the immersed-finite-element particle-in-cell (IFEPIC) code discussed in Refs. 49 and 55, the USC-IFEPIC. This code was previously applied in several ion thruster plume simulation studies.[36,37,56] The PIC model considers operation by two active thrusters, one emitting positively, and one emitting negatively. For numerical accuracy, we assume that positive and negative currents emitted by thruster pair are identical, $J_{EMI^+} + J_{EMI(EMI-BF_4)^+} = J_{BF_4^-} + J_{BF_4(EMI-BF_4)^-}$. The PIC model simulates the plume ejected by an entire thruster

TABLE I. Physical input parameters for PP model setup.

Parameter	Symbol	Value	Unit
Accelerating voltage	ϕ_0	±1 500	V
Pore radius	R_p	1	μm
Tip to extractor distance	d	49	μm
Cation monomer mass	m_{EMI^+}	117	g/mol
Cation dimer mass	$m_{EMI(EMI-BF_4)^+}$	309.15	g/mol
Anion monomer mass	$m_{BF_4^-}$	86.81	g/mol
Anion dimer mass	$m_{BF_4(EMI-BF_4)^-}$	284.79	g/mol
Particle charge	q	±1.6 × 10⁻¹⁹	C
Current	I	16	nA
Particle emission rate	$\dot{N}_d$	10¹¹	s⁻¹

TABLE II. Key simulation parameters in physical and normalized units.

Parameter	Physical units	Normalized units
$n_{0_{BF_4^-}}$	4.83×10^{12} 1/m^3	1.0
$T_{BF_4^-}$	10 eV	1.0
$\lambda_{D_{BF_4^-}}$	10.7 mm	1.0
$v_{th_{BF_4^-}}$	4690 m/s	1.0
m_{EMI^+}	111.17 g/mol	1.28
$m_{BF_4^-}$	86.81 g/mol	1.0
$m_{EMI(EMI-BF_4)^+}$	309.15 g/mol	3.56
$m_{BF_4(EMI-BF_4)^-}$	284.79 g/mol	3.28
dt	0.32 μs	0.01

consisting of many emitter tips. We assume that the values solved for a single emitter tip within the MD and PP models can be generalized to represent the emission profile of the entire array of a single thruster (i.e., all emitter tips in each thruster are identical). The particles from the PP model are sampled by the PIC model to determine the species composition and VDFs of particles entering the downstream region.

The simulation parameters are normalized to the BF_4^- anion with an assumed isotropic temperature $T_{0_{BF_4^-}} = 10$ eV and initial density $n_{0_{BF_4^-}} = 4.83 \times 10^{12}$ 1/m^3,

$$\hat{\mathbf{x}} = \frac{\mathbf{x}}{\lambda_{D_{BF_4^-}}}, \quad \hat{\mathbf{v}} = \frac{\mathbf{v}}{v_{th_{BF_4^-}}}, \quad \hat{t} = t\omega_{p_{BF_4^-}},$$

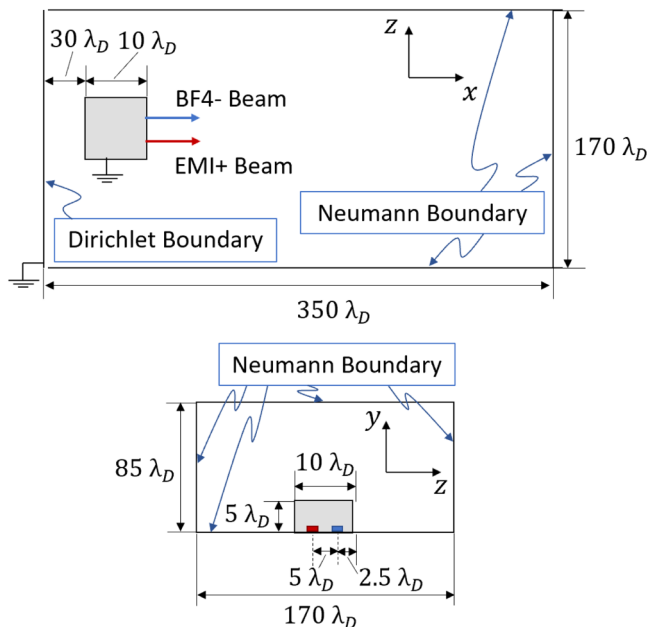$$\hat{m} = \frac{m_i}{m_{BF_4^-}}, \quad \hat{q} = \frac{q}{e}, \quad \hat{\Phi} = \frac{e\Phi}{k_b T_{BF_4^-}}, \tag{4}$$

FIG. 6. Simulation domain setup with boundary conditions. The red cell denotes the area of EMI^+ injection and the blue cells denote the area of BF_4^- injection.
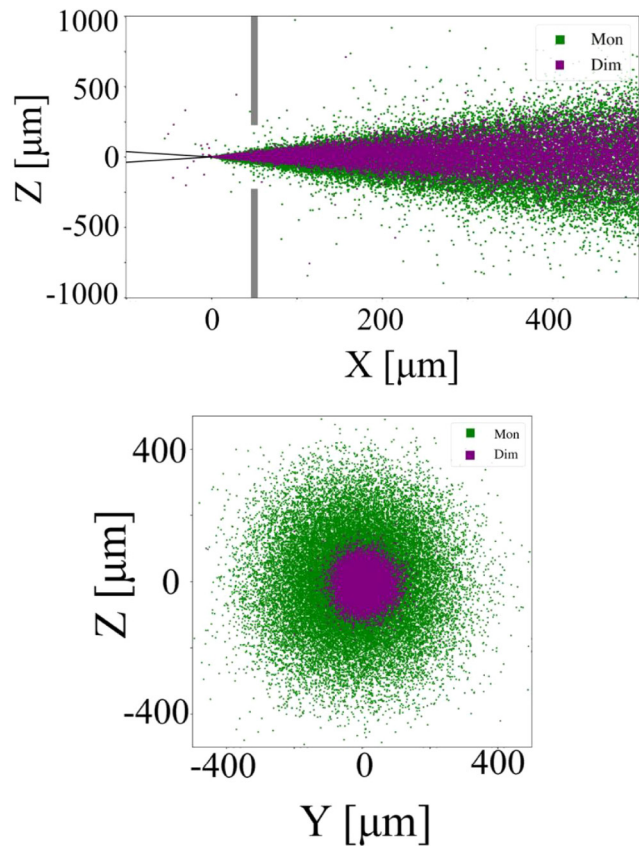
FIG. 7. Particle positions in the XZ plane (top) and YZ plane (bottom).

where

$$\lambda_{D_{BF_4^-}} = \sqrt{\frac{\varepsilon_0 k_b T_{BF_4^-}}{n_{0_{BF_4}} e^2}}$$

and

$$\omega_{p_{BF_4^-}} = \sqrt{\frac{n_{0_{BF_4}} e^2}{\varepsilon_0 m_{BF_4}}}$$

are the Debye length

and ion plasma frequency evaluated for BF_4^-, respectively. Table II shows key simulation parameters in both physical and normalized units. In this table, dt is the simulation time step.

Figure 6 shows the simulation domain and boundary conditions. The simulation considers a 1U size CubeSat with a thruster pair. As the charge density associated with the thruster beam is orders of magnitude larger than that of the ambient plasma, the effect of ambient electron and ion species are not included in this model. Given the current-free emission from the thruster pair, the spacecraft potential is assumed to be the same as the unperturbed

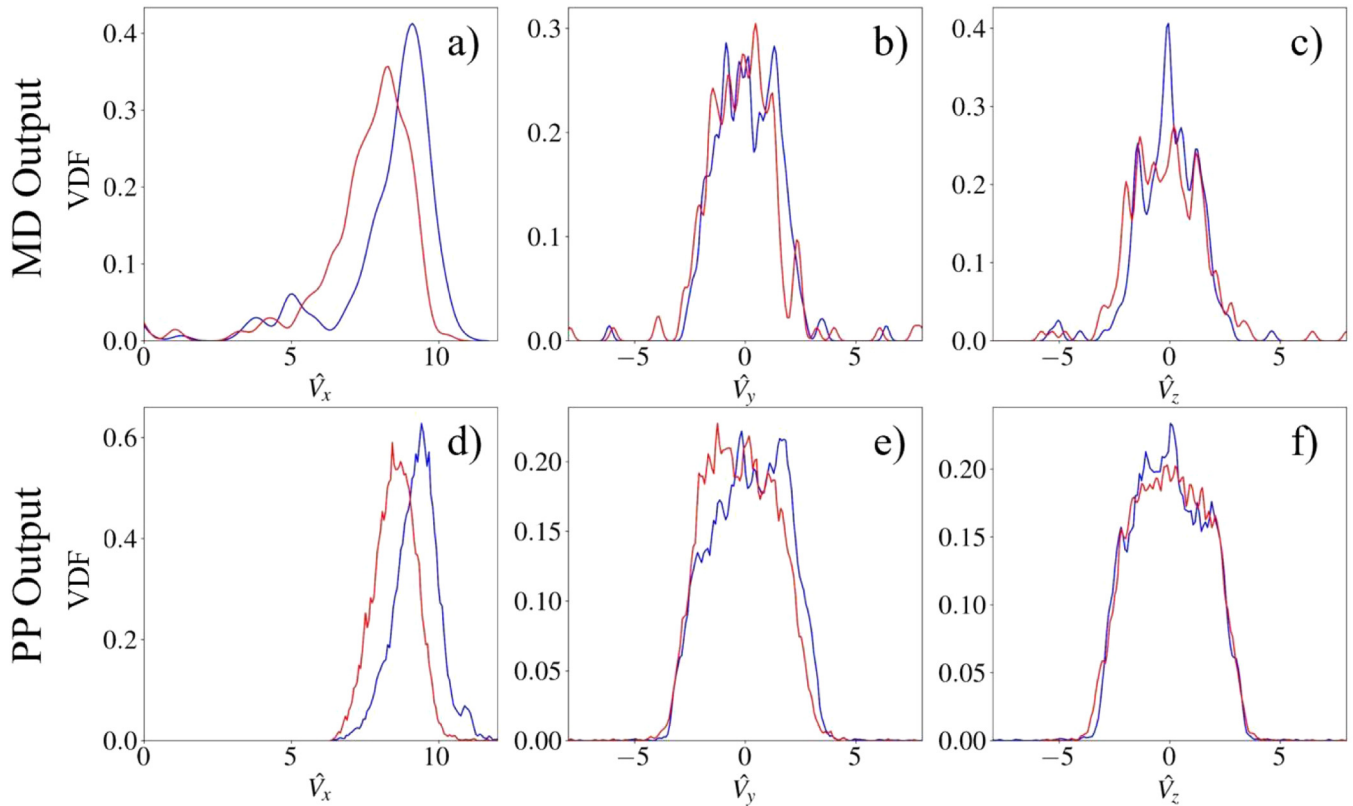**FIG. 8.** Comparison of monomer velocity distribution functions (VDFs) at the input (top) and output (bottom) of the PP model. Red denotes cation and blue denotes anion. Left: Velocity distribution in the X direction. Middle: Velocity distribution in the Y direction. Right: Velocity distribution in the Z direction.

ambient plasma. In the simulation, the upstream boundary represents the unperturbed ambient; thus, the potential of both the spacecraft and the upstream boundary is taken to be zero. The Neumann boundary condition is applied for the potential at all other domain boundaries. The simulation domain leverages midline symmetry and a mirrored boundary along the $-Y$ plane. The simulation is ended before significant portions of the injected beam ions reach the outer boundaries of the domain so to eliminate potential numerical effects from the domain boundary. The simulation domain size is also shown in Fig. 6. Test runs were carried out to ensure that the domain used is sufficiently large and has no influence on the results. The simulation domain has $350 \times 85 \times 170$ cells with a cell resolution $dx = dy = dz = \lambda_{D_{BF_4^-}}$. The CubeSat is represented by a cubic box of $10\lambda_{D_{BF_4^-}} \times 10\lambda_{D_{BF_4^-}} \times 10\lambda_{D_{BF_4^-}}$. The thruster exit area is $1\lambda_{D_{BF_4^-}} \times 1\lambda_{D_{BF_4^-}}$.

In the simulation, both cations and anions are represented by macro-particles. The electric field, particle trajectories, and space charge density are solved self-consistently from Poisson's equation and Newton's second law subject to the required boundary conditions,

$$-\nabla \hat{\Phi} = n_{EMI^+} + n_{EMI(EMI-BF_4)^+} - n_{BF_4^-} - n_{BF_4(EMI-BF_4)^-}, \quad (5)$$

$$\frac{d(\hat{m}\hat{\mathbf{v}})}{dt} = \hat{q}\hat{\mathbf{E}}. \quad (6)$$

At every time step, macro-particles representing the EMI and BF₄ monomers and dimers are injected into the simulation domain. The number of the macro-particles injected is 1692 for EMI^+, 1015 for $EMI(EMI-BF_4)^+$, 1914 for BF_4^-, and 1057 for $(EMI-BF_4)BF_4^-$. This injection rate is normalized but can relate to a physical current of 5.08 μA. Therefore, the PIC simulation represents a thruster consisting of approximately 318 distinct emitter tips. For the results displayed in Sec. III, the simulations all run for 2100 time steps. At the end of the simulation, the total number of macro-particles in the simulation domain is approximately 13×10^6. Each simulation takes approximately 3.5 days to run on the USC HPC.

III. RESULTS AND DISCUSSION

This section discusses results from multi-scale simulations to investigate (i) the physics and interactions at each scale of interest and (ii) the impact of activation of multiple emission sites at all scales. The results of the MD and PP sub-models are presented for both positive and negative thruster polarity. The PIC model combines these results to investigate beam neutralization with a bipolar
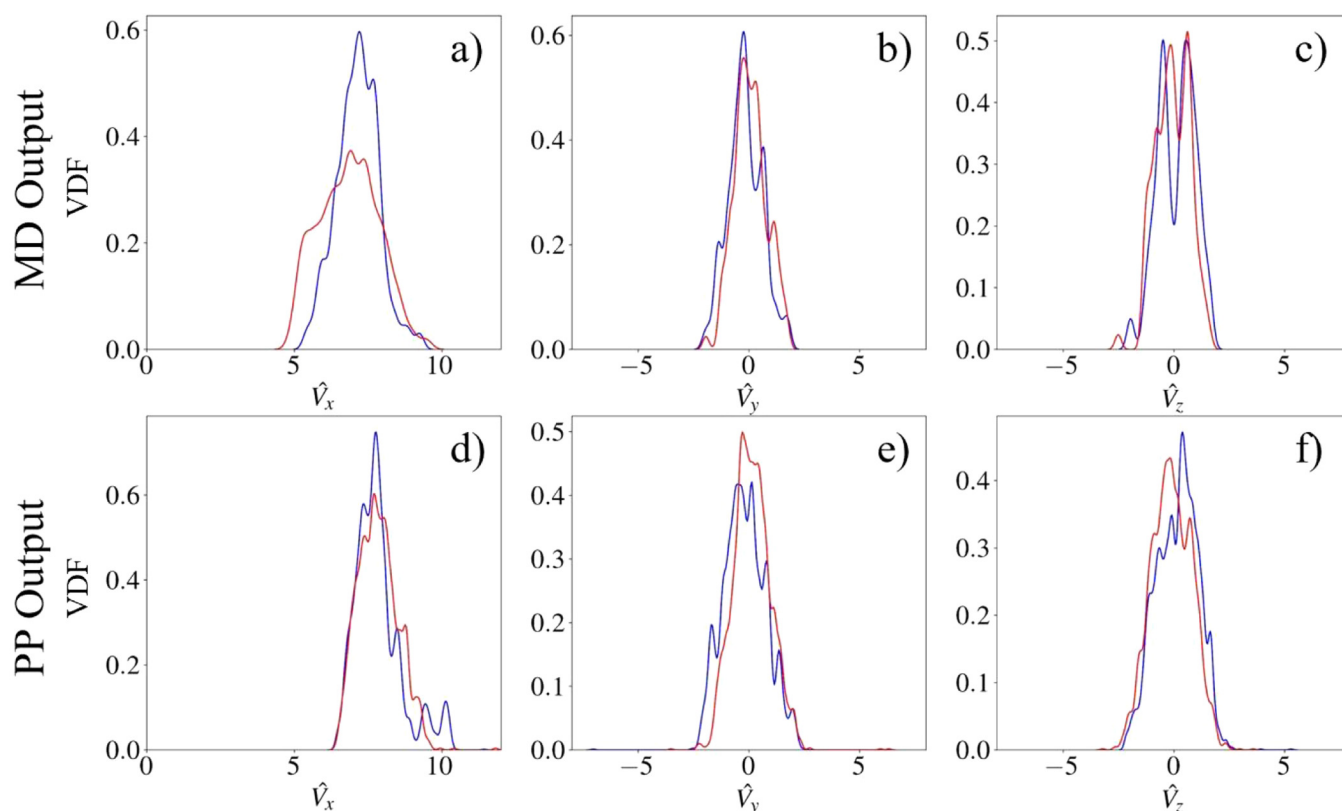
FIG. 9. Comparison of dimer velocity distribution functions (VDFs) at the input (top) and output (bottom) of the PP model. Red denotes cation and blue denotes anion. Left: Velocity distribution in the X direction. Middle: Velocity distribution in the Y direction. Right: Velocity distribution in the Z direction.

thruster pair. Due to randomness imposed by unknown pore locations within the substrate, and other unique micro-scale features and defects from emitter tip manufacturing, it is impossible to predict exactly where and when primary and secondary emission site will appear. However, this model allows for an example approach to make overall determinations into the effect of a secondary emission site if it is excited on a neighboring pore. Therefore, this simulation will present a series of results for a case with a single emission site as well as a case with a notional secondary or tertiary emission site activated on the side of the emitter tip.

A. Single emission site

The single emitter case considers that the particle velocity distribution function injected at the PP scale is consistent with that of the ± 2 V/nm MD emission case.

Figure 7 displays a positive cation plume consisting of monomers and dimer species along the XZ and YZ plane, respectively. Cartoon representations are included to roughly outline the physical positions of the emitter tip and the extractor grid with respect to the plume. It is important to note that the PP model does not include the extractor grid structure and, therefore, does not remove particles that intercept the extractor grid. Here, we can see that the

more mobile, lower mass monomer species experience a larger spread than the higher mass dimer species in the cross-beam, or Z direction. Additionally, it is noted that the overall scatter of the beam is slightly asymmetric. This asymmetry is likely introduced by the particle initialization provided by the MD model.

Figures 8 and 9 display particle velocity distribution functions from the input and output of the PP model. Both positive and negative emission modes are displayed for each figure. Focusing on Fig. 8 (panel a), we find that the MD model produces a sizeable fraction of low velocity monomers that have fragmented during the emission process. This is most easily seen by the second peak in the V_x distribution. Looking to the output of the PP model (panel d), we find that traversing through the acceleration region helps us to homogenize the resulting beam. Comparing panels b to e and panels c to f, it is noted that the fraction of outliers in the V_y and V_z component are reduced as well. Looking at Fig. 9, one can see in panels b, c, e, and f that the emitted dimer species are emitted with less variation in their cross-beam velocity components, another contributor to their occupancy of the beam's core. We can also see the significant acceleration of the dimer species along the X direction by comparing panels a and d. Comparing panel d of both Figs. 8 and 9, the PP output of V_x for both the monomers
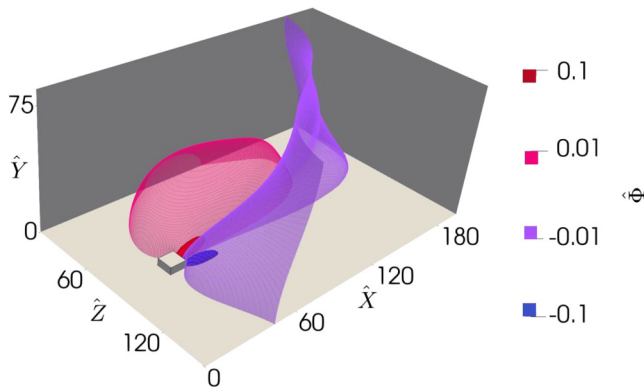
FIG. 10. Plasma potential contours for single emitter case.

FIG. 12. Electric field strength and vectors for single emitter case.

and dimers, it appears that the positive beam achieves a more homogeneous exit velocity than the negative beam. The fact that the positive monomers and dimers are proximate in exit velocity implies that we cannot assume that species accelerate independently. This beam homogeneity is achieved sometime during or just after the thruster exit plane.

The PP output can then be used to inject into the PIC model. Previous studies investigating the downstream region[44–46] assumed that the particle beam was well represented by an isotropic Maxwellian distribution drifting in the X direction. Looking at Figs. 8 and 9 (panels d, e, and f), we can see that this previous assumption is inaccurate. The V_y and V_z component, while comparable, provide a very steep decline for large velocities. The following figures display the results of the 3D PIC model focused on the general structure of the downstream region. All figures are presented as an isometric view of the data within the 3D domain.

Figures 10–12 display results of the downstream plume PIC model. Figure 10 displays the normalized plasma potential with logarithmic contours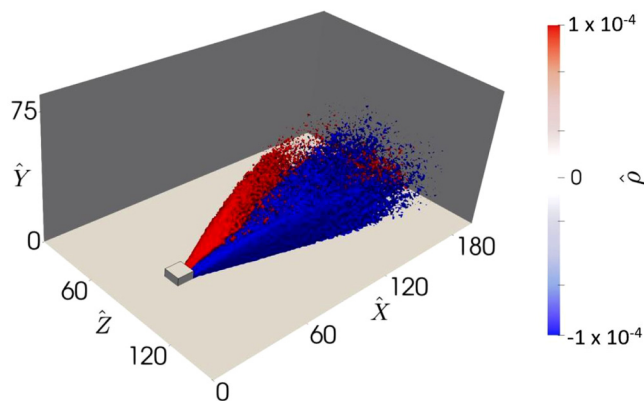 at ± 0.1 and ± 0.01. These contours are semi-transparent to display the nested nature. Red contours denote areas of positive potential and blue contours denote areas of negative potential. Figure 11 displays the normalized charge density also with logarithmic contours at $\pm 1 \times 10^{-4}$. The red contours denote regions of positive net charge density and the blue contours denote regions of negative net charge density. The contours span from ± 0.1 to $\pm 1 \times 10^{-5}$. Figure 12 displays the normalized electric field. The figure includes arrows denoting the electric field vectors throughout the domain. Note that the displayed arrows are of constant length and that any variations in the perceived vector length is due to foreshortening by out-of-plane field components. The magnitude of the electric field is captured by the color bar. A 2D slice displaying portions of the XY plane and corresponding electric field vectors is provided to capture the 3D structure of the electric field.

The overall features of the plume are very similar to those previously reported. In general, the downstream plume behavior displays relatively little coupling between the positive and negative beams. The plasma potential and electric field strength are slight, amounting to a maximum of ± 2.8 V and 113 V/m, respectively. As a result, the beam expansion occurs relatively unimpeded. Upon comparing Figs. 10–12 to previous results, we can see the overall beam spread is larger along the Z direction but smaller in the Y direction. There are also very small populations of the beam that
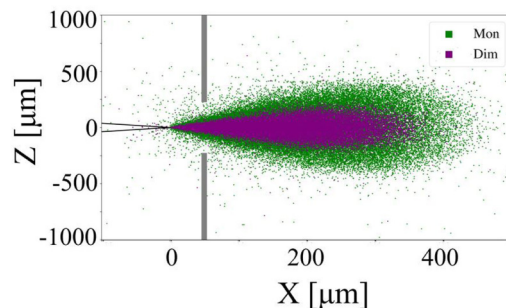

FIG. 11. Charge density contours for single emitter case.

FIG. 13. PP model particle positions in XZ plane for two emitter case.
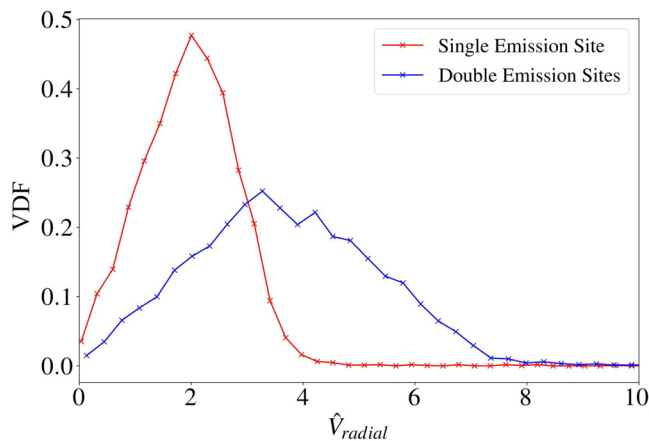
FIG. 14. Comparison of beam-radial velocity distribution between single emitter and double emitter case.

FIG. 15. Plasma potential contours for triple emitter case.

leave the thruster at large angles. Despite these differences, the overall neutralization process of the beam appears to not be adversely affected.

B. Effects of multiple emission sites

The multiple emitter case introduces a secondary emission site at $5\,\mu$m from the center-line. This distance corresponds to an activation of the closest neighboring pore, assuming average porosity. This case is analyzed in the MD and PP models, and results are displayed below. Due to the symmetry in the PIC model, a triple emitter case was also tested, which introduced two secondary sites $\pm 5\,\mu$m from the center-line. We assume the primary emission site has an extraction field of 2 V/nm and that any additional emission sites experience a lesser electric field of 1.5 V/nm. Figure 13 displays particle positions for the XZ plane for the two emitter case.

Comparing Figs. 7 and 13, one can see the scattering induced by the activation of a secondary emission site. Both the monomer and dimer portions of the beam experience an increased spread along the beam-radial direction. Figure 14 compares the beam-radial velocity distribution for the single and double emitter cases. The average radial velocity of the particles is increased as well as the standard deviation, with the max radial velocity almost doubling. Activation of the second emission site increases the number of particles capable of impacting the extractor grid, leading to losses of thrust and grid contamination.

PIC model results are presented for a triple emitter case. Figures 15–17 display the relevant plasma parameters as an isometric view once more. These plots are displayed in the same style discussed previously in the single emitter case results. Here, we can see that despite the increase in overall spreading, the primary downstream neutralization mechanisms are maintained. The max electric field strength and potential are comparable to that of the single emitter case. The primary difference between the two cases is the increased expansion angle of the beam. Otherwise, it does not appear that the presence of multiple emission sites per tip adversely affects the beam neutralization process.
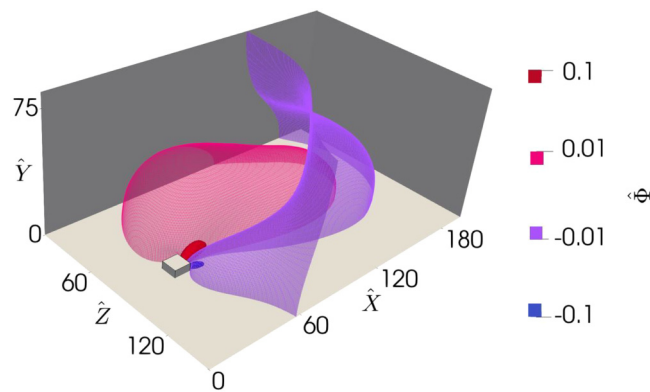
C. Discussions

The simulation results suggest that prior model assumptions that the beam species are accelerated independently is inaccurate. The exact composition of the cation or anion beam will affect the acceleration of each particle as they experience inter-particle forces in the acceleration region. In addition, the distribution of the beam-radial velocity components were shown to not strictly follow a Maxwellian distribution. Furthermore, high mass species, such as dimers, trimers, tetramers, or droplets, if emitted on-axis, experience less radial spreading and are more likely to be found in the core of the beam. Results from the downstream region PIC model imply that inclusion of MD and PP model physics do not adversely affect beam neutralization. The overall physical interactions between the positive and negative beams are largely similar and comparable to the simplified models previously examined. Adequate neutralization exists wherever the densities of the individual thrusters are opposing and equal. Overall, this model further affirms the conclusions presented previously by the simplified
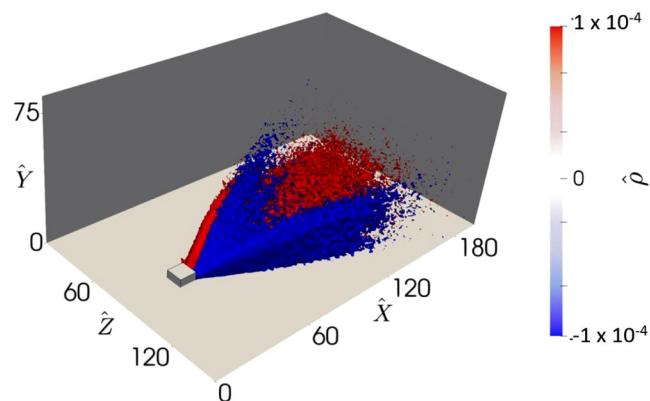

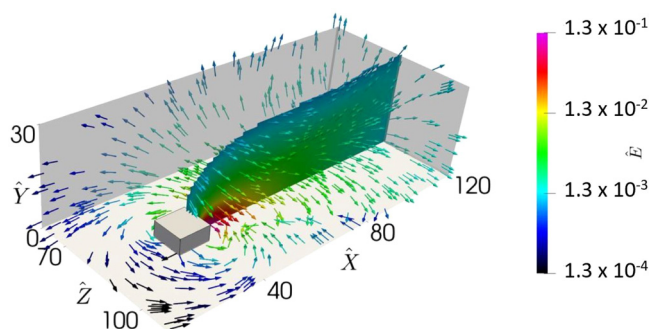**FIG. 16.** Charge density contours for triple emitter case.

FIG. 17. Electric field strength and vectors for single emitter case.

downstream model[46] while providing further insight into how lower-level physics adjusts the primary mechanisms observed.

The impact of secondary site emission has been documented before experimentally[21] but the underlying interactions between multiple beams within the acceleration region has not yet been well understood. The introduction of a second or third emission site on a single emitter tip is likely more dangerous for a thruster than it is beneficial. The presence of multiple emission sites causes a marked increase in the overall expansion of the individual beamlets. This increases the likelihood of contamination or destruction of the critical extractor electrode. Despite the adverse affects of secondary site activation at the acceleration region scale, there are less noticeable adverse affects inhibiting beam neutralization in the downstream region.

IV. CONCLUSIONS AND FUTURE WORK

Accurate understanding of ion emission, acceleration, and neutralization physics is critical in estimating thruster performance and lifetime-limiting effects as well as larger scale impacts to spacecraft surface contamination and ambient plasma interactions. The paper presents, to our knowledge, the first combined MD, PP, and PIC simulations of the ion emission, acceleration, and neutralization processes for an ionic electrospray thruster with porous emitter tips using EMI-BF$_4$ ionic liquid propellant. Results are presented on key characteristics of the interaction that take place during the development of the ionic electrospray thruster plume from O (nm), O (μm), O (cm), to O (m) length scales.

A major conclusion from this study pertains to the insight gained from investigating multiple emission sites from a single emitter tip. In general, the activation of multiple emission sites on a single emitter tip increases the likelihood for grid interception and increases the overall beam half angle. Specifically, we noted an increased spread of velocity distributions along the same axis that contained the secondary emission site. This model is the first to be able to resolve the full three-dimensional particle dynamics to better understand how multiple beams can mix, interact, and ultimately affect the current collection on the extractor electrode. To fully understand the impact to a unique thruster, a dedicated joint numerical and experimental characterization effort is needed to determine thresholds for nominal operation. Factors such as

tip-to-extractor geometry, substrate porosity, and manufacturing defects will likely contribute significantly to overall results.

Results show that the overall plume dynamics in the downstream region are similar to that of previous PIC simulations using idealized beams.[46] We reaffirm that the downstream region exhibits small electric fields and that the resulting patterns are driven largely by superposition of the two expanding beams. Since the electric field in the downstream region does little to affect the overall particle trajectory, the resulting features reflect the injected distribution functions output by the acceleration region. Therefore, interactions at the acceleration region scale can cause subtle changes within the macroscopic plume.

This study represents a first attempt to develop a multi-scale model of ionic electrospray emission. Several important issues still need to be addressed in future study. For instance, ion fragmentation within the acceleration region was not assessed completely in the current model. Fragmentation from the emission process was included in the MD model but no other particles were allowed to fragment in the acceleration or field-free region. The acceleration region was capable of accelerating these fragmented particles to the beam energy. Future work will need to include energy loss mechanisms, such as ion fragmentation in the acceleration region and field-free region, as observed by Miller.[57,58] These empirical models can readily be included in future simulations, given the existing framework. It is important to understand in future work if the particle–particle forces within the beam core is enough to sufficiently scatter the lower energy monomer species produced from dimer-to-monomer fragmentation during acceleration. Additionally, the acceleration physics and momentum transfer between beam components in the acceleration region need to be investigated further. The extent to which monomers interact with higher mass particles in the plume and the effect of composition on performance are critical to furthering this model and our understanding of ionic electrospray thruster physics.

AUTHOR DECLARATIONS

Conflict of Interest

The authors have no conflicts to disclose.

Author Contributions

J. Asher and Z. Huang contributed equally to this work.

DATA AVAILABILITY

The data that support the findings of this study are available from the corresponding author upon reasonable request.

REFERENCES

[1] M. Natisin, H. Zamora, W. McGhee, N. Arnold, Z. Holley, M. Holmes, and D. Eckhardt, "Fabrication and characterization of a fully conventionally machined high-performance porous media electrospray thruster," J. Micromech. Microeng. **30**, 115021 (2020).

[2] C. Chen, M. Chen, and H. Zhou, "Characterization of an ionic liquid electrospray thruster with a porous ceramic emitter," Plasma Sci. Technol. **22**, 094009 (2020).

[3] E. M. Petro, A. R. Bruno, and P. C. Lozano, "Characterization of the TILE electrospray emitters," in *AIAA Propulsion and Energy Forum*, August 24–28, 2020 (American Institute of Aeronautics and Astronautics, 2020).

[4] C. Ma and C. Ryan, "Plume characterization of a porous electrospray thruster," in *Proceedings of the 36th International Electric Propulsion Conference*, Vienna, Austria, Sept. 15–20, 2019 (Electric Rocket Society, 2019).

[5] T. Fedkiw, Z. Wood, N. Demmons, and D. Courtney, "Environmental and lifetime testing of the bet-300-p electrospray thruster," in *AIAA Propulsion and Energy 2020 Forum*, August 24–28, 2020 (American Institute of Aeronautics and Astronautics, 2020).

[6] G. Taylor, "Disintegration of water drops in an electric field," Proc. R. Soc. Lond. Ser. A **280**, 383–397 (1964).

[7] M. Gamero-Castaño and J. Fernández De La Mora, "Mechanisms of electrospray ionization of singly and multiply charged salt clusters," Anal. Chim. Acta **406**, 67–91 (2000).

[8] D. G. Courtney, H. Q. Li, and P. Lozano, "Emission measurements from planar arrays of porous ionic liquid ion sources," J. Appl. Phys. **45**, 485203 (2012).

[9] D. G. Courtney and H. Shea, "Fragmentation in time-of-flight spectrometry-based calculations of ionic electrospray thruster performance," J. Guid. Control Dyn. **38**, 1500–1504 (2015).

[10] C. Coffman, L. Perna, H. Li, and P. C. Lozano, "On the manufacturing and emission characteristics of a novel borosilicate electrospray source," in *Proceedings of the 49th AIAA/ASME/SAE/ASEE Joint Propulsion Conference*, San Jose, CA, July 14–17, 2013 (American Institute of Aeronautics and Astronautics, 2013), Vol. 1, Pt. F.

[11] R. S. Legge and P. C. Lozano, "Electrospray propulsion based on emitters microfabricated in porous metals," J. Propul. Power **27**, 485–495 (2011).

[12] A. Thuppul, P. L. Wright, A. L. Collins, J. K. Ziemer, and R. E. Wirz, "Lifetime considerations for electrospray thrusters," Aerospace **7**, 108 (2020).

[13] A. G. Hsu, B. B. Brady, M. P. Easton, A. C. Labatete-goeppinger, T. J. Curtiss, D. Krejci, and P. Lozano, "Laboratory testing of a modular 8-thruster scalable ion electrospray propulsion system," in *Proceedings of the 36th International Electric Propulsion Conference*, Vienna, Austria, Sept. 15–20, 2019 (Electric Rocket Society, 2017).

[14] F. Mier-Hicks and P. C. Lozano, "Spacecraft-charging characteristics induced by the operation of electrospray thrusters," J. Propul. Power **33**, 456–467 (2017).

[15] D. Krejci, F. Mier-Hicks, R. Thomas, T. Haag, and P. Lozano, "Emission characteristics of passively fed electrospray microthrusters with propellant reservoirs," J. Spacecr. Rockets **54**, 447–458 (2017).

[16] J. E. Polk, J. R. Brophy, J. Wang, and S. Diego, "Spatial and temporal distribution of ion engine accelerator grid erosion," in *Proceedings of the 31st AIAA/ASME/SAE/ASEE Joint Propulsion Conference and Exhibit*, San Diego, CA, July 10–12, 1995 (American Institute of Aeronautics and Astronautics, 1995).

[17] J. R. Brophy, I. Katz, J. E. Polk, and J. R. Anderson, "Numerical simulations of ion thruster accelerator grid erosion," in *Proceedings of the 38th AIAA/ASME/SAE/ASEE Joint Propulsion Conference and Exhibit*, Indianapolis, IN, July 7–10, 2002 (American Institute of Aeronautics and Astronautics, 2002).

[18] J. W. Emhoff and I. D. Boyd, "Grid erosion modeling of the next ion thruster optics," in *Proceedings of the 39th AIAA/ASME/SAE/ASEE Joint Propulsion Conference and Exhibit*, Huntsville, AL, July 20–23, 2003 (American Institute of Aeronautics and Astronautics, 2003).

[19] R. E. Wirz, J. R. Anderson, D. M. Goebel, and I. Katz, "Decel grid effects on ion thruster grid erosion," IEEE Trans. Plasma Sci. **36**, 2122–2129 (2008).

[20] M. Nakano, "Three-dimensional simulations of grid erosion in ion engines," Vacuum **83**, 82–85 (2008).

[21] C. Guerra-Garcia, D. Krejci, and P. Lozano, "Spatial uniformity of the current emitted by an array of passively fed electrospray porous emitters," J. Phys. D: Appl. Phys. **49**, 115503 (2016).

[22] R. E. Wirz, A. L. Collins, A. Thuppul, P. L. Wright, N. M. Uchizono, H. Huh, M. J. Davis, J. K. Ziemer, and N. R. Demmons, "Electrospray thruster performance and lifetime investigation for the LISA mission," in *AIAA Propulsion and Energy Forum and Exposition*, Indianapolis, IN, August 19–22, 2019 (American Institute of Aeronautics and Astronautics, 2019).

[23] J. Zhang, G. Cai, X. Liu, B. He, and W. Wang, "Molecular dynamics simulation of ionic liquid electrospray: Revealing the effects of interaction potential models," Acta Astronaut. **179**, 581–593 (2021).

[24] A. Borner and D. A. Levin, "Coupled molecular dynamics—3D Poisson simulations of ionic liquid electrospray thrusters," IEEE Trans. Plasma Sci. **43**, 295–304 (2015).

[25] N. A. Mehta and D. A. Levin, "Molecular dynamics electrospray simulations of coarse-grained ethylammonium nitrate (EAN) and 1-ethyl-3-methylimidazolium tetrafluoroborate (EMIM-BF4)," Aerospace **5**, 1–18 (2018).

[26] N. A. Mehta and D. A. Levin, "Sensitivity of electrospray molecular dynamics simulations to long-range Coulomb interaction models," Phys. Rev. E **97**, 1–13 (2018).

[27] A. Borner, Z. Li, and D. A. Levin, "Modeling of an ionic liquid electrospray using a molecular dynamics model," AIP Conf. Proc. **1501**, 887–894 (2012).

[28] A. Borner, Z. Li, and D. A. Levin, "Prediction of fundamental properties of ionic liquid electrospray thrusters using molecular dynamics," J. Phys. Chem. B **117**, 6768–6781 (2013).

[29] T. M. Coles and P. C. Lozano, "Investigating efficiency losses from solvated ion fragmentation in electrospray thruster beams," in *Proceedings of the 49th AIAA/ASME/SAE/ASEE Joint Propulsion Conference*, San Jose, CA, July 14–17, 2013 (American Institute of Aeronautics and Astronautics, San Jose, CA, 2013), Vol. 1, Pt. F.

[30] J. Rosell-Llompart, J. Grifoll, and I. G. Loscertales, "Electrosprays in the cone-jet mode: From Taylor cone formation to spray development," J. Aerosol. Sci. **125**, 2–31 (2018).

[31] Y. Zhao and J. J. Wang, "A particle-particle simulation model for droplet acceleration in colloid thrusters," in *Proceedings of the 36th International Electric Propulsion Conference*, Vienna, Austria, Sept. 15–20, 2019 (Electric Rocket Society, Vienna, 2019).

[32] K. Emoto, T. Tsuchiya, and Y. Takao, "Numerical investigation of steady and transient ion beam extraction mechanisms for electrospray thrusters," Trans. Jpn. Soc. Aeronaut. Space Sci. **16**, 110–115 (2018).

[33] R. I. Samanta Roy, D. E. Hastings, and N. A. Gatsonis, "Ion-thruster plume modeling for backflow contamination," J. Spacecr. Rockets **33**, 525–534 (1996).

[34] I. D. Boyd, "Review of Hall thruster plume modeling," J. Spacecr. Rockets **38**, 381–387 (2001).

[35] J. Wang and D. Brinza, "Three-dimensional particle simulations of ion propulsion plasma environment for Deep Space 1," J. Spacecr. Rockets **38**, 433–440 (2001).

[36] J. Wang, Y. Cao, R. Kafafy, J. Pierru, and V. Decyk, "Simulations of ion thruster-plume-spacecraft interactions on parallel supercomputer," IEEE Trans. Plasma Sci. **34**, 2148–2158 (2006).

[37] R. Kafafy and J. Wang, "A hybrid grid immersed finite element particle-in-cell algorithm for modeling spacecraft—Plasma interactions," IEEE Trans. Plasma Phys. **34**, 2114–2124 (2006).

[38] J. Wang and Y. Hu, "On the limitations of hybrid particle-in-cell for ion thruster plume simulations," Phys. Plasmas **26**, 103502 (2019).

[39] M. Tajmar and J. Wang, "Three-dimensional numerical simulation of field-emission-electric-propulsion neutralization," J. Propul. Power **16**, 536–544 (2000).

[40] M. Tajmar and J. Wang, "Three-dimensional numerical simulation of field-emission-electric-propulsion backflow contamination," J. Spacecr. Rockets **38**, 69–78 (2001).

[41] J. F. Roussel, T. Tondu, J. C. Matéo-Vélez, E. Chesta, S. D'Escrivan, and L. Perraud, "Modeling of FEEP plume effects on MICROSCOPE spacecraft," IEEE Trans. Plasma Sci. **36**, 2378–2386 (2008).

[42]A. J. Lopez-Arreguin and E. Stoll, "Addressing the effects of background plasma and wake formation on nanosatellites with electric propulsion using a 3D particle in cell code," Results Phys. **14**, 102442 (2019).

[43]D. G. Courtney, H. Shea, K. Dannenmayer, and A. Bulit, "Charge neutralization and direct thrust measurements from bipolar pairs of ionic electrospray thrusters," J. Spacecr. Rockets **55**, 54–65 (2018).

[44]C. Cui and J. Wang, "Simulations of pure ionic electrospray thruster plume neutralization," in *AIAA Propulsion and Energy 2020 Forum*, *August 24–28, 2020* (American Institute of Aeronautics and Astronautics, 2020).

[45]J. S. Asher and J. Wang, "On the impact of ion fragmentation on bipolar ionic electrospray thruster pair operations: 3D PIC simulations," in *AIAA Propulsion and Energy Forum*, *August 9–11, 2021* (American Institute of Aeronautics and Astronautics, 2021).

[46]J. S. Asher and J. Wang, "3-dimensional particle-in-cell simulations of bipolar ionic electrospray thruster plume," J. Propul. Power (to be published, 2021).

[47]R. J. Antypas and J. J. Wang, "Pure ionic electrospray extractor design optimization," in *Proceedings of the 36th International Electric Propulsion Conference, Vienna, Austria, Sept. 15–20, 2019* (Electric Rocket Society, Vienna, 2019).

[48]R. Kafafy, T. Lin, Y. Lin, and J. Wang, "Three-dimensional immersed finite element methods for electric field simulation in composite materials," Int. J. Numer. Methods Eng. **64**, 940–972 (2005).

[49]D. Han, P. Wang, X. He, T. Lin, and J. Wang, "A 3D immersed finite element method with non-homogeneous interface flux jump for applications in particle-in-cell simulations of plasma-lunar surface interactions," J. Comput. Phys. **321**, 965–980 (2016).

[50]M. J. Abraham, T. Murtola, R. Schulz, S. Páll, J. C. Smith, B. Hess, and E. Lindah, "GROMACS: High performance molecular simulations through multi-level parallelism from laptops to supercomputers," SoftwareX **1–2**, 19–25 (2015).

[51]A. P. Thompson, H. M. Aktulga, R. Berger, D. S. Bolintineanu, W. M. Brown, P. S. Crozier, P. J. in 't Veld, A. Kohlmeyer, S. G. Moore, T. D. Nguyen, R. Shan, M. J. Stevens, J. Tranchida, C. Trott, and S. J. Plimpton, "LAMMPS—A flexible simulation tool for particle-based materials modeling at the atomic, meso, and continuum scales," Comp. Phys. Comm. **271**, 108171 (2022).

[52]F. Zhang, X. Jiang, G. Chen, Y. He, G. Hu, and R. Qiao, "Electric-field-driven ion emission from the free surface of room temperature ionic liquids," J. Phys. Chem. Lett. **12**, 711–716 (2021).

[53]N. Takahashi, "Molecular dynamics modeling of ionic liquids in electrospray propulsion," Technical Report (Massachusetts Institute of Technology, Cambridge, 2010).

[54]Y. Zhao, J. Wang, and H. Usui, "Simulations of ion thruster beam neutralization using a particle-particle model," J. Propul. Power **34**, 1109–1115 (2018).

[55]J. Wang, D. Han, and Y. Hu, "Kinetic simulations of plasma plume potential in a vacuum chamber," IEEE Trans. Plasma Sci. **43**, 3047–3053 (2015).

[56]J. Wang, P. Wang, M. Belhaj, and J. C. Mateo Velez, "Modeling facility effects on secondary electron emission experiment," IEEE Trans. Plasma Sci. **40**, 2773–2780 (2012).

[57]C. E. Miller and P. C. Lozano, "Measurement of the fragmentation rates of solvated ions in ion electrospray thrusters," in *Proceedings of the 52nd AIAA/SAE/ASEE Joint Propulsion Conference*, *Salt Lake City, UT, July 25–27, 2016* (American Institute of Aeronautics and Astronautics, 2016).

[58]C. E. Miller, "Characterization of ion cluster fragmentation in ionic liquid ion sources," Ph.D. thesis (Massachusetts Institute of Technology, 2019).